Article

Synthesis, Physicochemical, Thermal and Antioxidative Properties of Zn(II) Coordination Compounds with Pyrazole-Type Ligand

Berta Barta Holló [1,*] ![ORCID], **Mirjana M. Radanović** [1] ![ORCID], **Marko V. Rodić** [1] ![ORCID], **Sanja Krstić** [1] ![ORCID], **Željko K. Jaćimović** [2] ![ORCID] and **Ljiljana S. Vojinović Ješić** [1] ![ORCID]

1   Department of Chemistry, Biochemistry and Environmental Protection, Faculty of Sciences, University of Novi Sad, 21000 Novi Sad, Serbia; mirjana.lalovic@dh.uns.ac.rs (M.M.R.); marko.rodic@dh.uns.ac.rs (M.V.R.); sanja.vlaisavljevic@dh.uns.ac.rs (S.K.); ljiljana.vojinovic-jesic@dh.uns.ac.rs (L.S.V.J.)

2   Faculty of Metallurgy and Technology, University of Montenegro, 81000 Podgorica, Montenegro; zeljkoj@ucg.ac.me

*   Correspondence: hberta@uns.ac.rs

Abstract: The reactions of pyrazole derivative, i.e., ethyl-5-amino-1-methyl-1*H*-pyrazole-4-carboxylate (**L**) with zinc halogenides in methanolic solution and zinc nitrate and zinc acetate in acetonic solution are described. The formulae of synthesized compounds are ZnL_2Cl_2 (**1**), $[ZnL_2Br_2]$ (**2**), $ZnL_2I_2 \cdot 0.5MeOH$ (**3**), $[Zn(L)_2(H_2O)_4](NO_3)_2$ (**4**), and $\{ZnL(OAc)_2\}_2$ (**5**). Two complexes are obtained in form of single crystals: $[ZnL_2Br_2]$ (**2**) and $[Zn(L)_2(H_2O)_4](NO_3)_2$ (**4**). Their crystal and molecular structure were determined by single-crystal X-ray structure analysis. The FTIR spectra of compounds prove the complex formation with all five zinc salts. The complexes are characterized by conductometric and thermoanalytical measurements, and their antioxidative activity was also tested by the scavenging effect on the DPPH radical. Conductometric results, solvolytic stability, and antioxidative activity of the compounds are in correlation.

Keywords: pyrazole-type ligand; Zn complex; synthesis; structure; thermal decomposition; antioxidative activity

1. Introduction

Pyrazole derivatives and their coordination complexes are longer in the focus of research because of their applicability in a wide range. A great number of pyrazole derivatives show antimicrobial [1–4], anti-inflammatory [5–8], antipyretic [8], or antitumor activity. Besides, pyrazole-type compounds due to their good coordination ability and small molecules are very useful for modeling active centers and enzymatic or other biochemical reactions [9,10]. The wide range of their bioactivity is also presented by pyrazole-type active components of some pesticides [11–14]. However, not only the biological activity of pyrazoles and their metal complexes is important. This family of compounds is characterized by relatively high thermal stability and easy chemical bond formation under proper conditions. Therefore, pyrazoles also can give porous metal-organic frameworks and coordination polymers [15,16]. Besides, they are also important precursors for chemical vapor deposition processes. Some pyrazole-based compounds show good catalytic properties [10,17], while others with nitrogen-rich substituents are candidates for energetic materials [18,19].

In accordance, the potentially biologically active pyrazoles and their transition metal complexes are longer in the focus of our research group [20–23]. For the systematic design of biologically active compounds, their detailed physical and chemical characterization is necessary, as well as the determination of their thermal stability. Sometimes the thermal

properties of compounds can correlate with their biological activity. It can be useful in the examination of the mechanism of their bioactivity.

In this paper, we continue our earlier research and describe the synthesis of three new complexes of ethyl-5-amino-1-methyl-1H-pyrazole-4-carboxylate (**L**) with zinc halogenides, ZnX_2, X = Cl, Br, I of general formula ZnL_2X_2 with X = Cl and Br (**1** and **2**) and $ZnL_2I_2 \cdot 0.5MeOH$ (**3**). Furthermore, **L** with $Zn(NO_3)_2 \cdot 6H_2O$ gives $[Zn(L)_2(H_2O)_4](NO_3)_2$ (**4**), and with $Zn(OAc)_2 \cdot 2H_2O$ gives $\{ZnL(OAc)_2\}_2$ (**5**). The compounds were characterized by standard methods of elemental analysis, conductometry, IR spectroscopy, and TG-DSC measurements. Additionally, the compounds were tested for the scavenging effect on the DPPH radical (DPPH•) to determine their antioxidative activity. The crystal and molecular structure of the $[ZnL_2Br_2]$ (**2**) and $[Zn(L)_2(H_2O)_4](NO_3)_2$ (**4**) was determined by single-crystal X-ray structure analysis.

2. Results and Discussion

2.1. Syntheses and Physicochemical Properties of the Complexes

In the reaction zinc(II)-halogenides and warm methanolic solutions of the ligand in a mole ratio 1:2, bis(ligand) complexes of the formula $Zn(L)_2X_2$, X = Cl, Br (**1–2**) and $Zn(L)_2I_2 \cdot 0.5MeOH$ (**3**) are obtained. Salts zinc acetate and zinc nitrate did not give solid reaction products from methanolic solutions. Therefore, these syntheses were repeated in a few solvents and single crystals of $[ZnL_2(H_2O)_4](NO_3)_2$ (**4**) and the microcrystalline complex compound $\{ZnL(OAc)_2\}_2$ (**5**) were obtained from acetonic solutions of their reaction mixtures. The scheme of the synthesis is presented in Scheme 1. In complexes **1–3**, the central ion is tetracoordinated with two monodentate pyrazole-type ligands and two halogenide ions, which is, in the case of complex **2**, confirmed by single-crystal XRD analysis (vide infra). Pyrazole-type ligand is coordinated in a monodentate manner, through the N1 nitrogen atom, as it was found in the recently characterized structure of copper(II) complex [20]. The monodentate coordination of two molecules of pyrazole-type ligand was found in complex **4** as well, while the other four coordination places are occupied with water molecules giving the octahedral surroundings to the central ion.
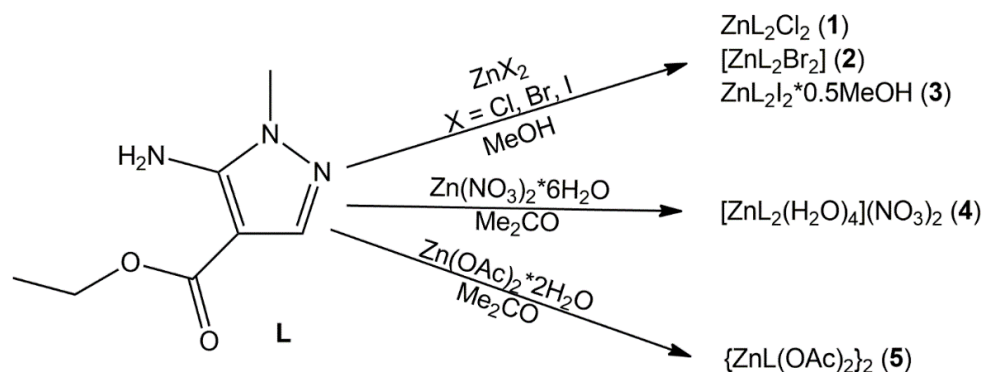
Scheme 1. Synthesis of zinc complexes (**1**)–(**5**).

Complexes **1** and **5** are white and complex **3** is a yellow microcrystalline substance, while complexes **2** and **4** are obtained in the form of colorless plate-like single-crystals. All the obtained compounds are stable in air. The compounds are well soluble in DMF, poorly soluble in MeOH, and insoluble in H_2O and EtOH. Therefore, their molar conductivity was measured in DMF solutions. Molar conductivity data for **1**, **2,** and **5** prove their nonelectrolyte type, while the conductivity of iodido complex (**3**) has the value which corresponds to electrolytes between types 1:1 and 2:1, which indicates instability of this complex in DMF solution, i.e., dissociation of voluminous iodido ligands [24]. Molar conductivity value of **4** (130 S cm^2 mol^{-1}) is characteristic for electrolytes type 2:1 and is in concordance with the coordination formula. Compared to the analogous CuL_2X_2 (X = Cl and Br) complexes described earlier [20], the values of molar conductivity of **1** and **2** are significantly lower

than that of corresponding Cu compounds. These data show higher stability of Zn compounds in DMF solution. The significantly lower stability of **3** in DMF can be explained by the dimensions of halogenides. Based on its position in the periodic table it could be easily concluded that Cl^- and Br^- can be placed in the coordination sphere more comfortably with less repulsion than I^-. Due to larger dimensions of I^-, they are closer to each other and to the coordinated pyrazoles, which causes higher repulsions between them and easier dissociation in solution. Conductivity values of **4** and **5** are like that for analogous Cu-complexes [20]. Due to the structural properties of acetate ion, it easily forms bridges and gives dimeric salts. Such structure was observed in the case of $[Cu(L)(\mu\text{-OAc})_2]_2$ described in our previous paper [20]. Almost the same molar conductivity values of **5** (3.5 S cm^2 mol^{-1}) and $[Cu(L)(\mu\text{-OAc})_2]_2$ (3.4 S cm^2 mol^{-1}) suggest high solvolytic stabilities of both compounds and structural similarity between them.

2.2. Crystal Structure of Complexes **2** and **4**

The molecular structures of the complexes are presented in Figure 1, while the selected structural parameters are given in Table 1.
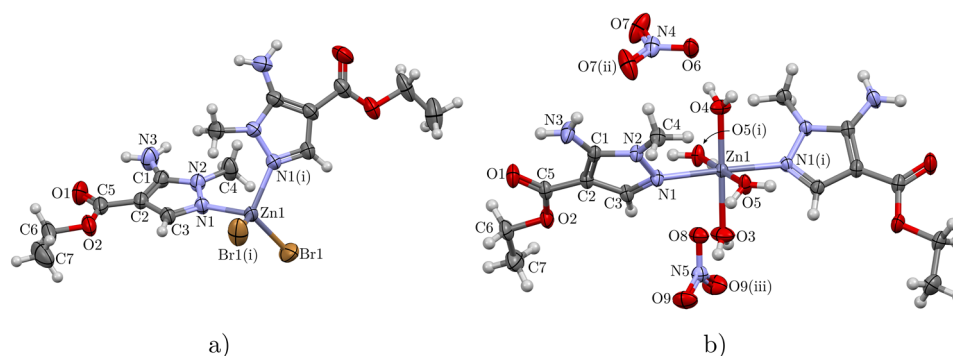

Figure 1. Molecular structures of (**a**) $[Zn(L)_2Br_2]$ (**2**); (**b**) $[Zn(L)_2(H_2O)_4](NO_3)_2$ (**4**). Ellipsoids are drawn at 50 percent probability level. Symmetry operations: (i) $-x + 1, -y + 1, -z + 1$ (**2**) and $-x + 1, -y + 1/2, z$ (**4**); (ii) $x + 3/2, y, -z + 1$; (iii) $-x, -y + 1/2, z$.

Table 1. Selected structural parameters of $[Zn(L)_2Br_2]$ (**2**), and $[Zn(L)_2(H_2O)_4](NO_3)_2$ (**4**).

Bonds	Length, Å		Bonds	Angle, °	
	2	**4**		**2**	**4**
Zn1–N1	2.034 (2)	2.1977 (12)	N1–Zn1–N1 ^{i}	102.16 (14)	178.34 (6)
Zn1–Br1	2.3498 (4)	–	N1–Zn1–Br1	108.13 (7)	–
Zn1–O3	–	2.1028 (18)	N1 ^{i}–Zn1–Br1	108.83 (7)	–
Zn1–O4	–	2.0655 (16)	Br1–Zn1–Br1 ^{i}	119.39 (3)	–
Zn1–O5	–	2.0833 (10)	O5–Zn1–O5 ^{i}	–	179.61 (6)
O1–C5	1.207 (4)	1.2152 (19)	O4–Zn1–O3	–	180
O2–C5	1.329 (4)	1.3399 (19)			
O2–C6	1.453 (4)	1.4567 (19)			
N1–C3	1.321 (4)	1.3177 (19)			
N1–N2	1.382 (3)	1.3890 (16)			
N2–C1	1.342 (4)	1.3470 (18)			
N2–C4	1.446 (4)	1.4505 (18)	C5–O2–C6	117.2 (3)	115.78 (12)
N3–C1	1.346 (4)	1.340 (2)	C3–N1–N2	105.9 (2)	104.79 (11)
C1–C2	1.401 (4)	1.402 (2)	C3–N1–Zn1	129.2 (2)	121.98 (10)
C2–C3	1.392 (4)	1.398 (2)	N2–N1–Zn1	124.51 (18)	127.08 (8)
C2–C5	1.449 (4)	1.4466 (19)	C1–C2–C5	125.7 (3)	124.68 (14)
C6–C7	1.479 (7)	1.496 (3)			

Symmetry operations: ^{i} $-x + 1, -y + 1, -z + 1$ (**2**) and $-x + 1, -y + 1/2, z$ (**4**).

Complex **2** crystallizes in the monoclinic system, in the *C*2/*c* space group. The asymmetric unit of **2** consists of half the complex molecule, since the Zn1 atom lies at a twofold symmetry axis that bisects Br1–Zn1–Br1(i) angle. The metal center in **2** is situated in slightly deformed tetrahedral surroundings of two pyrazole ligand molecules and two bromide anions. The amount of deformation can be judged by a four-coordinate geometry index, τ_4 [25], which has a value of 0.95.

Complex **4** crystallizes in the orthorhombic crystal system, in the *Ibca* space group. The asymmetric unit of **4** contains half of the cation $[ZnL_2(H_2O)_4]^{2+}$ and halves of two NO_3^- ions. All three structural fragments occupy special positions located on three mutually perpendicular twofold symmetry axes. In the complex cation, atoms O3, O4, and Zn1 lie on the symmetry element, while atoms N4 and O6 of one nitrate ion, as well as N5 and N8 of the other nitrate ion, occupy special positions. The central ion in **4** is hexacoordinated to two molecules of the pyrazole-type ligand and four molecules of water in an almost ideal octahedral environment with trans-angles values near the theoretical value (178.34(6)–180°).

In both complexes, the pyrazole-like ligand is coordinated in a neutral form in a monodentate mode, via N1 nitrogen atom, as it was found in the first complex with this ligand [20]. Both ligand molecules show a high degree of planarity, with the most pronounced rotation about C2–C5 bond (τ(C3–C2–C5–O1) = −174.8(3)° in **2** and 176.1(1)° in **4**). The dihedral angle between the planes of the ligands is 62° in **2** and 74° in **4**. The survey of CSD revealed 244 structures of zinc complexes in which the central ion is in the octahedral environment of four water molecules and two N-donor ligands. Comparison of these structures to complex **4** showed accordance considering the values of bond lengths and trans-angle values.

The crystal structure of **2** can be rationalized with the aid of Hirshfeld surface analysis and subsequent interaction energy calculation, which offer more insight into the real structural determinants than simple geometrical analysis of crystal packing [26,27]. The summary of intermolecular interaction energies of the unique molecular pairs constituting the first molecular coordination sphere for **2** calculated using the CE-HF energy model is given in Table 2. The complex molecule is surrounded by six neighboring molecules occupying the *bc* crystallographic plane (Figure 2a). Intermolecular interaction energies between these six pairs are the strongest in the crystal structure and are classified into three types, with two pairs in each.

Table 2. Summary of intermolecular interaction energies of the unique molecular pairs constituting the first molecular coordination sphere for **2** calculated using the CE-HF energy model.

Label	n	Symmetry Operation	R/Å	E/kJ mol^{-1}				
				E_{ele}	E_{pol}	E_{dis}	E_{rep}	E_{tot}
1	2	x, y, z	7.47	−64.7	−19.1	−33.5	29.3	−84.8
2	2	$-x + 1/2, -y + 1/2, -z$	13.22	−0.8	−1.6	−28.7	11.5	−18.5
3	2	$-x + 1/2, -y + 1/2, -z$	12.89	−20.9	−6.0	−16.5	12.2	−30.2
4	4	$x + 1/2, y + 1/2, z$	8.37	8.0	−7.6	−14.4	6.7	−4.4
5	2	$-x, -y, -z$	10.21	−9.8	−8.3	−61.5	21.3	−53.5
6	2	$-x, -y, -z$	13.00	−43.5	−12.4	−14.0	22.9	−46.4

Note. n is the number of interactions; R is the distance between molecular centroids. The relevant space group symmetry operation is reported without translation. $E_{tot} = k_{ele}E_{ele} + k_{pol}E_{pol} + k_{dis}E_{dis} + k_{rep}E_{rep}$, where k_{ele} = 1.019, k_{pol} = 0.651, k_{dis} = 0.901, and k_{rep} = 0.811 [28].

The strongest of them (E = −85 kJ mol^{-1}, label 1 in Table 2) is formed between translationally equivalent molecules forming a column parallel to crystallographic axis *b*, which is dominated by the electrostatic term. Visual inspection of the corresponding Hirshfeld surfaces (Figure 3) mapped with electrostatic potential (ESP) reveals perfect matching of patches with positive and negative ESP on neighboring surfaces, which explains stabilizing nature of this interaction. Corresponding Hirshfeld surfaces of the adjacent molecules are

populated with Br···H and H···H intermolecular contacts, but these are equal or longer than the sum of atoms' Van der Waals radii, as indicated by $d_{\text{norm}} \geq 0$ Å.
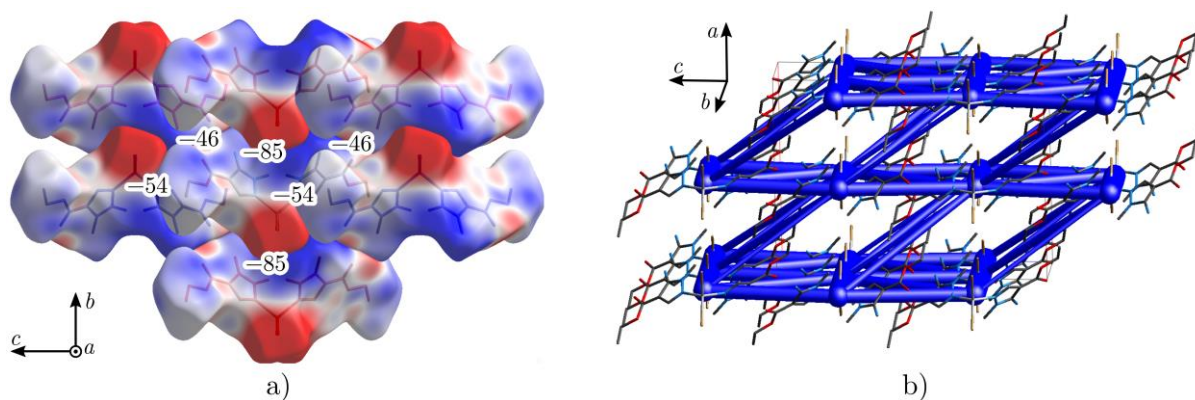

Figure 2. (**a**) Depiction of a layer of molecules in the crystallographic *bc* plane of **2** with Hirshfeld surfaces decorated with calculated electrostatic potential (ESP) in the range from −0.05 a.u. (red) to 0.05 a.u. (blue); Interaction energies are expressed in kJ mol⁻¹; (**b**) energy framework of the crystal structure **2** (interaction energies weaker than −10 kJ mol⁻¹ are omitted).
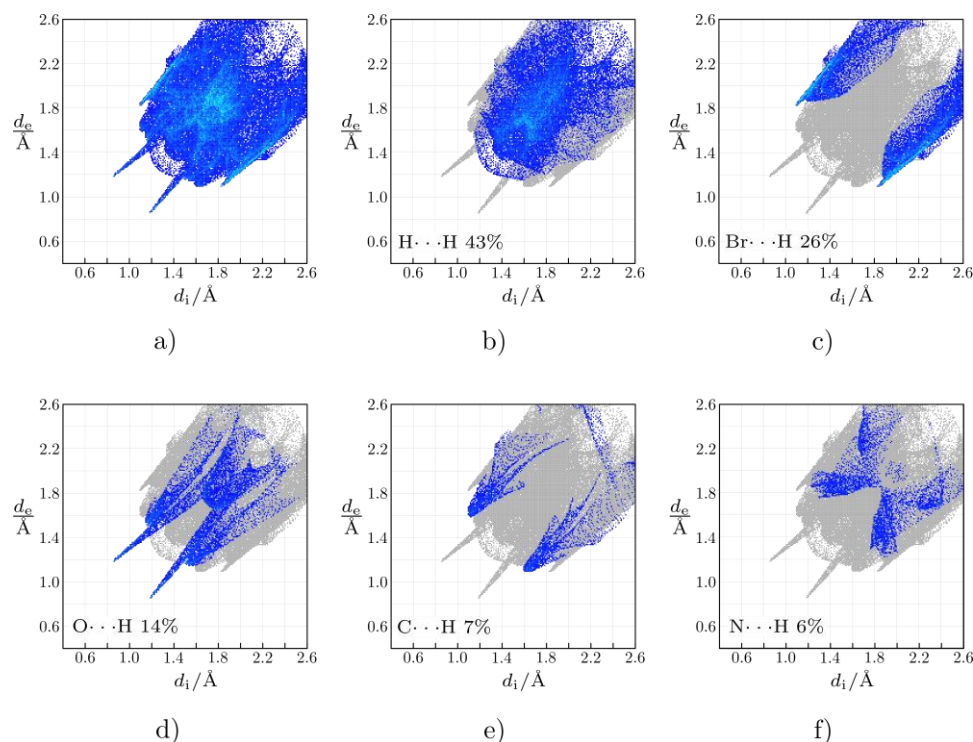

Figure 3. (**a**) Fingerprint plot of [Zn(L)$_2$Br$_2$] (**2**); (**b**)–(**f**) Fingerprint breakdown into element-specific contacts.

On the contrary, the next strongest interaction type ($E = -54$ kJ mol⁻¹, label 5 in Table 2) is dispersion dominated and has neglecting electrostatic contribution. These inversion-related interacting molecules form the largest contact area, comprising ca. 14% of the Hirshfeld surface. Corresponding to this interaction, N···H and O···H contacts are revealed in the HS breakdown, but these are characterized by $d_{\text{norm}} \geq 0$ Å.

The third ranked interaction type in the layer ($E = -46$ kJ mol⁻¹, label 6 in Table 2) is mediated through N3–H32···O1$^{\text{ii}}$ hydrogen bonds (symmetry operation (ii): $-x + 1$, $-y + 2$, $-z + 1$) and prevailingly has electrostatic character. This is in line with the pairing

of patches with positive ESP in the vicinity of NH_2 groups and patches with negative ESP in the proximity of C = O groups. Fingerprint plot shows spikes characteristic of O···H contact in hydrogen bonds.

Described molecular layers are stacked in direction of the c axis, where two types of stabilizing interactions are found, the stronger one ($E = -30$ kJ mol^{-1}, label 3 in Table 2), in which both electrostatics and dispersion play a significant role, and the weaker one ($E = -19$ kJ mol^{-1}, label 2 in Table 2), in which dispersion is dominant. Overall, the crystal structure of **2** can be considered as a layered one in the crystallographic *bc* plane, with stacking along the crystallographic *c* axis, which is visualized by the corresponding energy framework depicted in Figure 2b.

Since the crystal structure of **4** is predominantly ionic in nature, the calculation of intermolecular energies by the CE-HF method (used in complex **2**) is not suitable. Hirshfeld surfaces were calculated for all three constituents of the structure, and corresponding fingerprints are calculated and depicted in Figure 4. Hirshfeld surface analysis for complex cation $[ZnL_2(H_2O)_4]^{2+}$ reveals that O···H contacts are prominent in the crystals structure. They correspond to charge-assisted hydrogen bonds between coordinated water molecules and nitrate ions, as well as pyrazole ligand and nitrate ions. These hydrogen bonds constitute characteristic spikes in the fingerprint plots of the cation and the two independent nitrate anions.
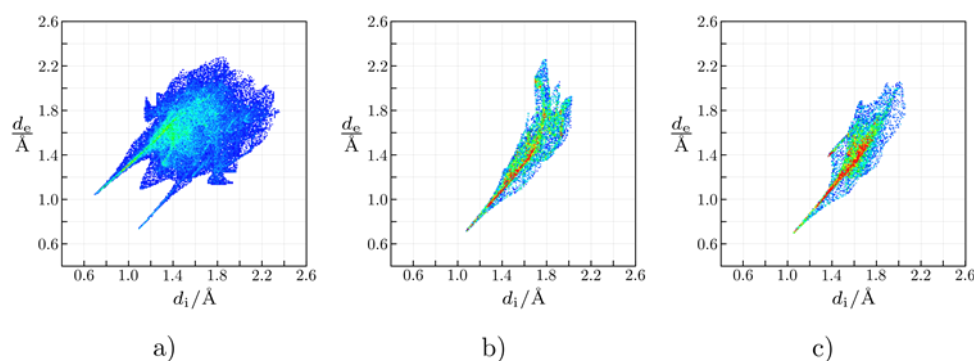

Figure 4. Fingerprint plots of ions in **2**: (**a**) complex cation $[ZnL_2(H_2O)_4]^{2+}$; (**b**) nitrate ion centered at N4; (**c**) nitrate ion centered at N5.

By examining the cation's Hirshfeld surface, it can be said that the complex cation is surrounded by 11 nitrate ions (Figure 5). Five of them are located in the proximity of the Zn atom, and in addition to Coulombic attraction, they interact with the cation through hydrogen bonds. Coordinated water molecules are hydrogen bond donors, while oxygen atoms of the nitrate ions are acceptors. Four nitrate ions are also involved in charge assisted hydrogen bonding but, in this case, amino groups of the pyrazole moiety play the role of hydrogen bond donors. Two additional nitrate ions, whose Hirshfeld surfaces touch with cation's Hirshfeld surface, are not involved in close atom–atom contacts.

Additionally, hydrogen bonds are formed between coordinated water molecule (centered at O5) as a donor, and carbonyl oxygen O1 ^{iv} (symmetry code as in Table 2). Hydrogen bond geometry is summarized in Table 3. Apart from hydrogen bonds, the fingerprint plot reveals CH···π interactions between methylene hydrogen atom within methoxy groups and pyrazole rings of the adjacent molecules. Finally, it is worth noting close approach of nitrate ions centered at N5, with O9···O9 ^{vii} distance of 2.751(2) Å (symmetry operation (vii): $-x - 1/2, -y + 1/2, -z + 1/2$), presumably because they are involved in hydrogen bonding with coordinated water molecules (centered at O3 and O5 atoms).
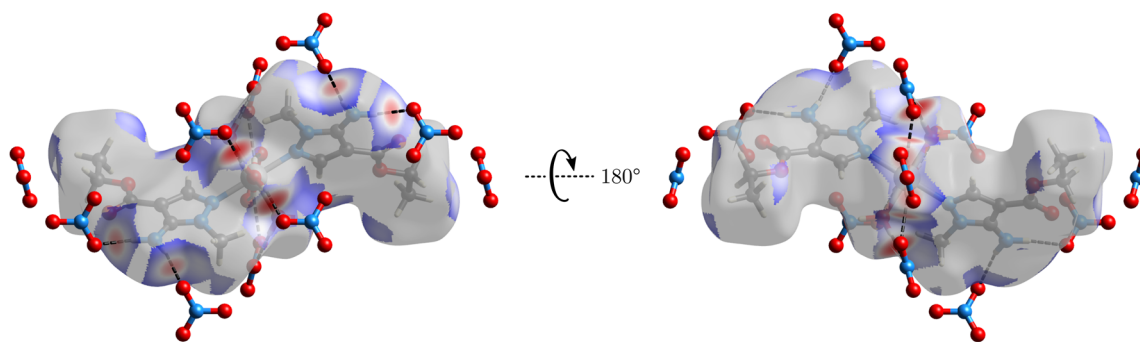
Figure 5. Hirshfeld surface of $[ZnL_2(H_2O)_4]^{2+}$ in **4**, decorated with d_{norm}, highlighting O···H contacts between the cation and surrounding nitrate anions. Color codes for decorating Hirshfeld surface are as follows: red—$d_{norm} < 0$; blue—$d_{norm} > 0$; white—$d_{norm} = 0$.

Table 3. Selected hydrogen-bond parameters in **4**.

D—H···*A*	*D*—H (Å)	H···*A* (Å)	*D*···*A* (Å)	*D*—H···*A* (°)
O3—H3C···O9 [i]	0.85	2.30	3.0894 (15)	154.6
O3—H3C···O9 [ii]	0.85	2.38	3.018 (2)	132.8
O4—H4A···O6 [iii]	0.84	1.94	2.7628 (11)	167.0
O5—H5A···O1 [iv]	0.82	1.99	2.7943 (15)	167.8
O5—H5B···O8	0.87	1.86	2.7201 (13)	171.6
O5—H5B···N5	0.87	2.62	3.4537 (17)	161.6
N3—H3A···O7 [v]	0.86	2.36	3.205 (2)	166.9
N3—H3B···O1	0.86	2.41	2.9539 (19)	121.2
N3—H3B···O7 [vi]	0.86	2.31	3.0138 (18)	139.2

Symmetry code(s): [i] $-x$, $-y + 1/2$, z; [ii] $x + 1/2$, y, $-z + 1/2$; [iii] $-x + 1$, $-y + 1/2$, z; [iv] $-x + 1/2$, $y-1/2$, z; [v] $x-1$, y, z; [vi] $-x + 1$, $-y + 1$, $-z + 1$.

2.3. FTIR Spectra of the Complexes

The spectra of the ligand and the coordination complexes are shown in Figure 6. As it can be seen, the spectrum of the pyrazole type ligand is somewhat different compared to the spectra of the complexes **1**–**5**. Observing the spectra of the complexes the similarity between them is obvious and suggests the same monodentate coordination of **L** to Zn. Taking into account the results of single-crystal XRD analysis and that zinc prefers tetracoordination, the geometry of all three halogenido compounds is most probably tetrahedral.

Due to coordination, the characteristic frequencies of ligands' bond vibrations are significantly changed. This leads to position and/or intensity changes of C–H, N–H bands in the range from ~3600–2800 cm^{-1}. The amino, methyl, and ethyl groups of the uncoordinated pyrazole ligand give strong bands at 3401, 3283, 3210, 3164, 3115, 2986 cm^{-1}, and medium bands 2940 and 2910 cm^{-1} (Figure 6). By coordination, the bands above 3000 cm^{-1} are shifted toward higher frequencies and the only strong bands are in the range from 3440–3430 and 3340–3337 cm^{-1}. The other bands in this IR range became less intensive due to the coordination of **L** to Zn. The C–H vibration bands from ~2870 to ~3000 cm^{-1} did not change their position, but their intensity is decreased by Zn–**L** bond formation. The freshly prepared **3** has given bands of significantly higher intensities at 3000–2800, 1449, and 1361 cm^{-1} compared to **1**, **2**, and **L** suggest the presence of MeOH. By storage, the lattice methanol evaporates, which causes the intensity decrease of the characteristic bands in the IR spectrum of **3** and bands of intensities like in the spectra of **1** and **2**. The differences between uncoordinated **L** and its complex compounds with zinc (**1**, **2**, **3**, **4**, and **5**) in shapes and intensities of bands in the ranges from 1500 to 1350 cm^{-1}; from 1050 to 800 cm^{-1} and bellow 750 cm^{-1} are caused by different inter- and intramolecular interactions and H-bonds in the crystal structure of **L** and compounds **1**, **2**, **3**, **4** and **5**.
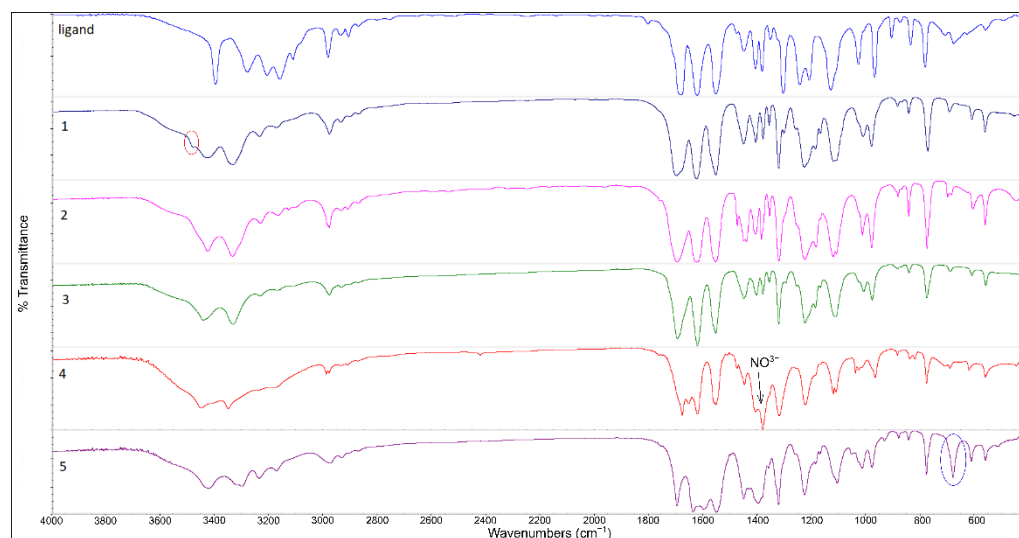
Figure 6. The FTIR spectra of the ligand and the complexes **1–5**.

Coordination complex **1** does not crystallize with lattice solvent but by coupled thermogravimetric-mass spectroscopic (TG-MS) measurements traces of absorbed water were found in its sample (see later). In its spectrum, a medium intensity band, overlapped with the next one was observed at 3484 cm^{-1} (Figure 6, marked with a red circle), which is missing from the other spectra. The other two halogenido complexes do not contain absorbed water, therefore this band may be the result of the presence of water traces. The absorbed water may affect the H-bonds in the crystal, which results in changed band shapes and gives O–H vibrations. In the spectra of halogenido compounds, the most intensive bands are in the range from 1700 to 1500 cm^{-1}.

The first four compounds contain coordinated anions as it is proved by single crystal XRD in the case of **2**, conductometric, and IR properties of the compounds. Differently, compound **4** was found by single-crystal XRD to contain four molecules of coordinated water. This water content causes differences in the IR spectrum of **4** from 3500 to 2800 cm^{-1} compared to **1–3** and **5**. Due to the H-bonds, the bands in this range are wider and more overlapped than the same bands in the other four spectra. By structural analysis we found that **4** contains nitrate ions in its outer coordination sphere. In accordance, the nitrates give a very intensive, characteristic band at 1384 and a small band at 824 cm^{-1} in its IR spectrum. These bands are in the range of uncoordinated nitrate [29]. In the spectrum of **4**, the "nitrate band" at 1384 cm^{-1} is the most intensive. Between 1700 and 1600 cm^{-1} there are three bands at 1682, 1657, and 1625 cm^{-1} but in this range of compounds **1–3** there are only two bands. The most probable reason for it is the different geometry and arrangement in the crystal lattice compared to halogenido complexes. The bands between 1100 and 900 cm^{-1} appear at somewhat different wavenumbers than in the other presented spectra. Since the pyrazole-type ligand is coordinated as a monodentate in all compounds, this difference is also caused by different molecular and crystal structures of **4**. The spectrum of **5** is somewhat different in the range 1700−1350 cm^{-1} due to the characteristic ν_s(OAc) and ν_{as}(OAc) bands of coordinated acetate at about 1400 and 1550 cm^{-1}, respectively [30]. Besides, an intensive band at 683 cm^{-1} was observed in the spectrum of **5** (Figure 6, marked with a blue circle). It is also characteristic for coordinated acetate.

2.4. Thermal Properties

For biologically active compounds is crucial to determine their thermal properties, thermal stability, decomposition mechanism, etc. Since complexes of Zn with ethyl-5-amino-1-methyl-1H-pyrazole-4-carboxylate (**L**) show significant antioxidative activity, for their future applicability it is necessary to examine their thermal properties. To see the effect of coordination on ligands thermal characteristics, its TG-DSC curves were compared with the

curves of compounds ZnL_2X_2 (X = Cl, Br; **1–2**), $ZnL_2I_2 \cdot 0.5MeOH$ (**3**), $[Zn(L)_2(H_2O)_4](NO_3)_2$ (**4**) and $\{ZnL(OAc)_2\}_2$ (**5**). In an inert atmosphere, ethyl-5-amino-1-methyl-1H-pyrazole-4-carboxylate (**L**) starts to decompose at 189 °C, onset, and up to 250 °C its decomposition is complete (Figure 7) as it was expected. The sharp endothermic peak on the simultaneous DSC curve shows that at the beginning of its decomposition, the ligand also melts. This was visually proved. The ligands' degradation is followed by the endothermic heat effect.
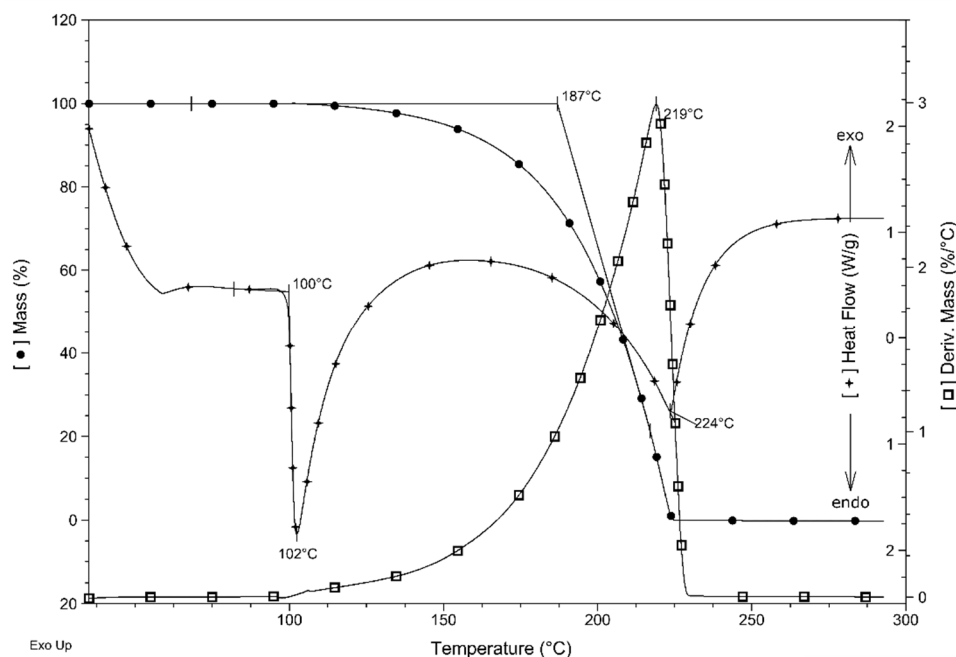

Figure 7. TG, DTG, and DSC curve of the ligand in nitrogen.

The thermal stability of coordination compounds of ethyl-5-amino-1-methyl-1H-pyrazole-4-carboxylate (**L**) with zinc halogenides (Figure 1a) increases with the increasing volume occupied by the anion. The DTG onset temperatures of **1–3** are 168, 177, and 179 °C, respectively. These values are in correlation with solvolytic stability, that is, the rate of substitution of coordinated anions by solvent molecules in a coordination complex. The solvolytic stability was determined by the molar conductivity of the compounds in DMF. The molar conductivity values are in inverse correlation with solvolytic stability. Therefore, the solvolytic stability of halogenido compounds increases in order **3 < 2 < 1**, which is the opposite order compared to their thermal stability. None of the halogenido complexes contains lattice solvent. The chloride complex (**1**) slowly loses 2.6% of its mass up to 130 °C, which is most probably adsorbed moisture from the atmosphere during storage because the elemental analysis data of freshly prepared compound does not show solvent content in the sample. On the other hand, the elemental analysis data show 0.5 molecule methanol in freshly prepared ZnL_2I_2 (**3**) but, during storage the methanol evaporated, and it was not detectable by thermoanalytical techniques. The complex compounds **1–3** decompose in several overlapped steps without stable intermediate formation. Most of their mass (about 50%) they lose up to 300 °C (Figure 8). The thermal decomposition of **1–3** does not finish up to 700 °C. At this temperature, a very low mass of samples remains, 10.3% (**1**), 5.6% (**2**), and 13.4% (**3**). These results show that in the case of **1** and **2** remains less mass than the zinc content of the samples (13.78% (**1**) and 11.60% (**2**)) and somewhat higher mass than the calculated zinc content (9.94%) in the case of **3**. Most probably by decomposition of ZnL_2X_2 some ZnX_2 is formed but metallic zinc, as well as ZnX_2 type zinc halogenides, melt at relatively low temperatures, namely Zn at 419.5, $ZnCl_2$ at 290, $ZnBr_2$ at 394, and ZnI_2 at 446 °C. In accordance, in a dynamic atmosphere, the formed zinc and zinc halogenide melts may evaporate. It may cause the solid remains' mass to be less than the mass of the zinc content of the compounds.
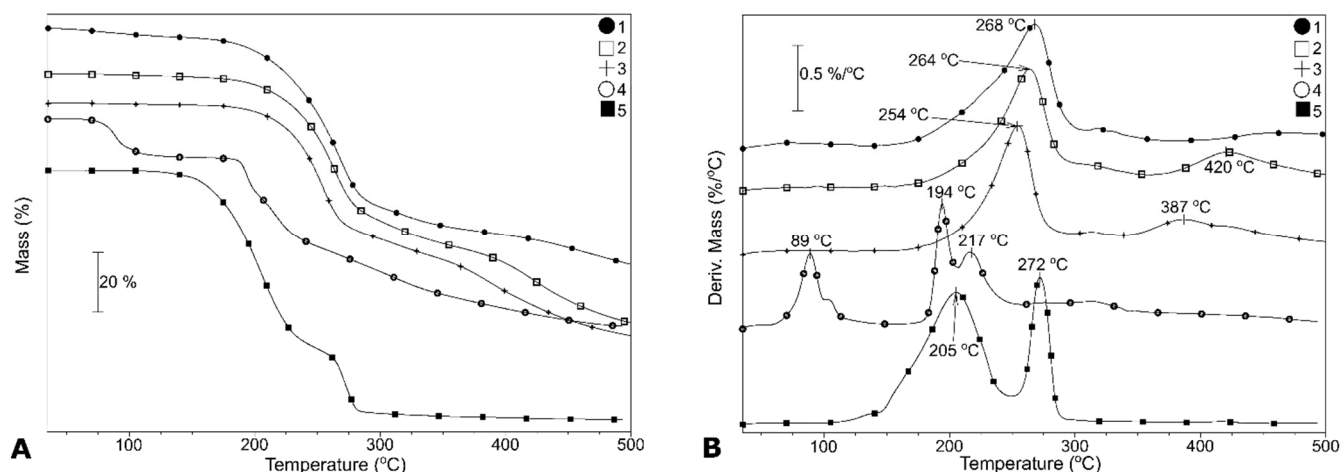
Figure 8. TG (**A**) and DTG (**B**) curves of complexes **1**–**5** in nitrogen.

Compared to the analog CuL_2X_2 compounds described earlier [20], where X = Cl (**1-Cu**) or Br (**2-Cu**), ZnL_2X_2 (X = Cl, Br, I) complexes are thermally less stable. Their thermal decomposition begins at a lower temperature than that of Cu compounds, but the most intensive decomposition processes of **1**–**3** take place at higher temperatures (DTG maxima at 268, 264, and 254 °C) than in the case of CuL_2Cl_2 and CuL_2Br_2 (DTG peaks at 229 and 221 °C). As it can be seen in Figure 9, decomposition of chlorido complexes of Zn and Cu above ~400 °C is less intensive and DTG peaks above this temperature can be observed only in the case of bromido and iodido coordination compounds.
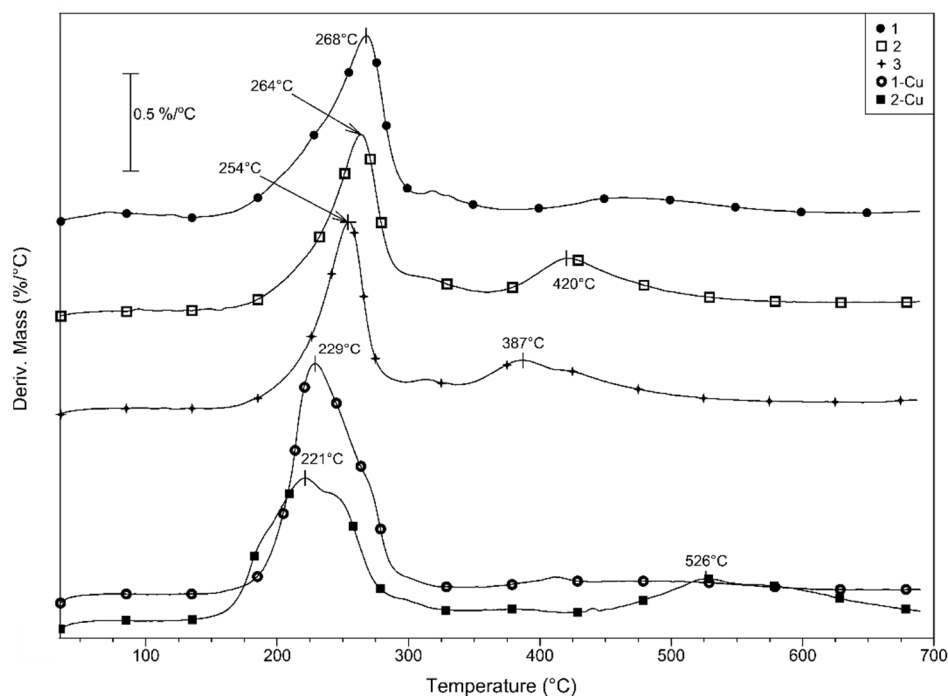

Figure 9. DTG curves of Zn complexes **1**–**3** and their Cu analogues **1**-Cu and **2**-Cu.

Compounds $[Zn(L)_2(H_2O)_4](NO_3)_2$ (**4**) and $\{ZnL(OAc)_2\}_2$ (**5**) decompose by a different mechanism compared to the halogenido complexes. Complex **4**, in accordance with its structure, firstly loses water. The dehydration begins at 62 °C, onset, and takes place in two steps (Figure 8) with DTG maxima at 89 °C, the mass loss is 9.8%, and at 104 °C with mass loss of 3.1%. These values correspond to the evaporation of somewhat more than

3 (9.0%) and 1 (3.0%) water molecules, respectively. These mass loss values suggest that compound **4** contains some adsorbed water too. The decomposition process of dehydrated **4** begins at 182 °C, onset, which is following the increased thermal stability with increasing volume occupied by anion, observed in the case of halogenido complexes. Its solvolytic stability is low, based on molar conductivity value, which is also in accordance with the opposite correlation between thermal and solvolytic stability observed earlier. The thermal decomposition of dehydrated **4** begins with a sharp DTG peak at 194 °C, which is overlapped with the next one at 216 °C. Nitrate easily decomposes at elevated temperatures, especially when it can oxidize the other ligand. The less thermally stable compound is complex **5** (170 °C, onset) with coordinated acetate. Its stability is higher than pure zinc acetate dihydrate and even the dehydrated zinc acetate, which decomposes in the temperature range between 150 and 320 °C [31]. Contrary to low thermal, the solvolytic stability of **5** is the highest compared to complexes **1–4**. Complex **5** decomposes in two well separated steps but without stable intermediate formation. The decomposition process is practically finished up to 300 °C. Above this temperature up to 500 °C only 2.1% of the mass is lost. The mass of final remains is somewhat less than the zinc content of the complex, which is following the findings in the case of halogenido compounds.

The heat effects of thermal decomposition of **1–3** up to ~400 °C are endothermic. The first endothermic peaks appear at 133 (**1**), 154 (**2**), and 184 °C (**3**) which shows increasing stability in order **1** < **2** < **3**. By visual observation we confirmed the melting of the samples at these temperatures, which means the decomposition begins with the melting of the samples. Below 300 °C, one more endothermic peak is observed on the DSC curves of **1–3**, which is in correlation with the highest mass loss process in all cases. Above 400 °C the heat flow curves show exothermicity. These results suggest that eventual evaporation processes take place between 200 and 300 °C and exclude the possibility of evaporation at higher temperatures (Figure 10).

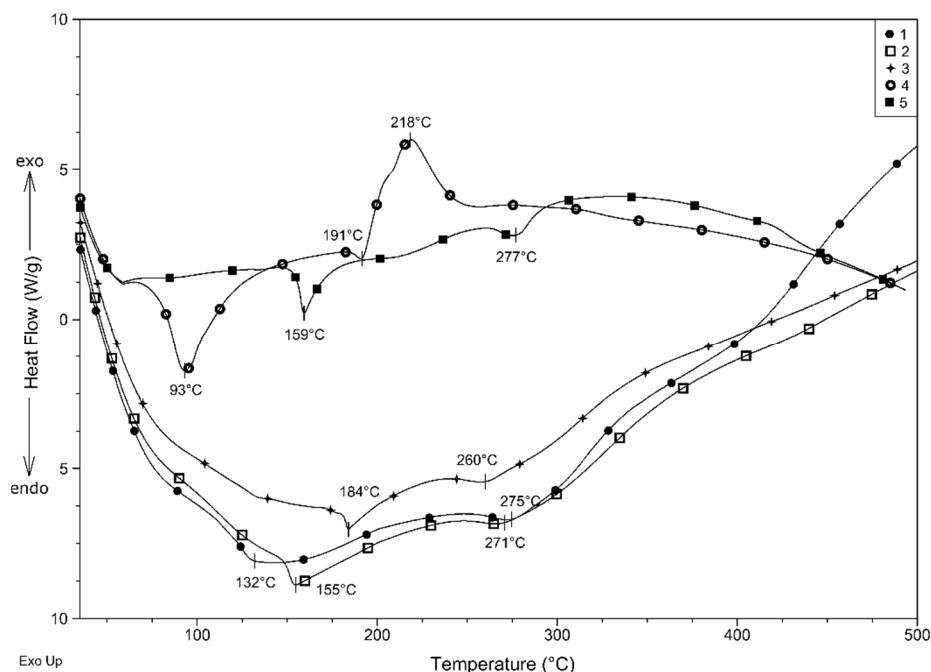**Figure 10.** DSC curves of complexes **1–5** in nitrogen.

The dehydration of complex **4** is endothermic as well as the beginning of the thermal decomposition of the complex with a DSC minimum at 191 °C. Above this temperature, the exothermic effect of nitrate decomposition is higher than the endothermicity of decomposition of coordinated **L** as was expected. The heat effect of complex **5**′s thermal decomposition

processes is endothermic up to ~400 °C. A small exothermic peak is observed at 419 °C, which may be correlated to oxidation processes.

To determine what is released from complex **1** above 100 °C, it was analyzed by coupled TG-MS measurement. Several fragments were detected with m/z values 17, 18, 29, 30, 43, and 44. The m/z = 17 and 18 signal intensity ratio (1:4) corresponds to water release [32]. This water may be absorbed moisture, but also a degradation product of pyrazole type ligand. Considering that mass of compound **1** decreases from ~60 °C, but the uncoordinated ligand starts to decompose at 100 °C, most probably at the beginning evaporates some absorbed water (Figure 11A). On the other hand, the fragments m/z = 29–44 detected at ~100 °C suggest that the decomposition of the pyrazole ligand has begun even when it is coordinated to Zn. The decomposition process also may result in some water formation. Signal with m/z = 29 most probably corresponds to $C_2H_5^+$ or CH_3N^+, 30 to CH_2O^+, while 43 to $C_2H_3O^+$. Fragment m/z = 44 may belong to CO_2^+ or N_2O^+. Since compound **1** does not contain oxidizing and reducing groups, N_2O^+ formation is most unlikely and fragment m/z = 44 belongs to CO_2^+ formed from the carboxylate group of **L**. It is supported by the low intensity of m/z = 30 compared to 44 also (Figure 11B). Namely, 30 m/z is an intensive characteristic signal for N_2O^+ fragment, but it is missing from the mass spectrum of CO_2.
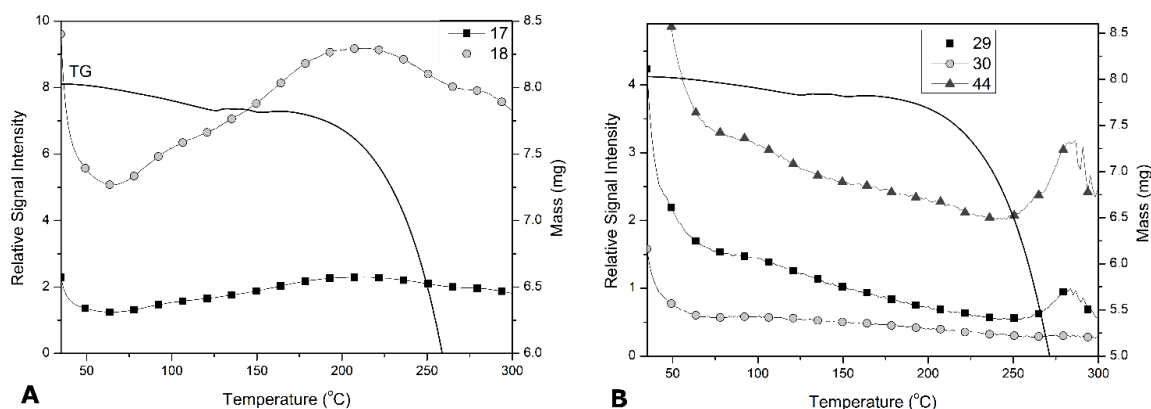

Figure 11. Fragments of water released from ZnL_2Cl_2 (**1**) in argon (**A**); Fragments of coordinated **L** in **1** in argon (**B**).

2.5. Antioxidative Capacity

The biological activity of pyrazole derivates has been extremely investigated in contrast to their complexes with transition metals [33]. Related to the greater bioactivity of this compound found in previous studies and favorable chemical characteristics of pyrazole derivates, new ideas have emerged for further investigations including the studies on zinc complexes with pyrazole ligand.

Thus, the aim of the present study was to evaluate the antioxidant activity of the zinc complexes with pyrazole-type ligand (**1**–**5**). This testing has been performed using DPPH (2,2-diphenyl-1-picrylhydrazyl) assay, created in vitro, and the ability of these samples to neutralize DPPH radical has been followed.

The results are presented in Figure 12.

Compound {$ZnL(OAc)_2$}$_2$ (**5**) (390.65 mg TE/g dsw) shows the best ability for radical neutralization followed by [ZnL_2Br_2] (**2**). On the other hand, the rest of the compounds $ZnL_2I_2 \cdot 0.5MeOH$ (**3**), [ZnL_2Cl_2] (**1**) and [$ZnL_2(H_2O)_4$](NO_3)$_2$ (**4**) exhibited similar activity, and **3** stood out (95.59 mg TE/g dsw). The high antioxidative activity of compounds **5** and **2** is in accordance with their high solvolytic stability (low molar conductivity). Namely, these compounds do not dissociate in DMF solutions, which suggests that they are highly stable in methanol too. During dissolution, compounds **3** and **4** dissociate to ions and show significantly lower antioxidative activities than **5** and **2**. Complex **1** shows low molar conductivity, which corresponds to high solvolytic stability but, differently to **5** and **2**, its antioxidative activity is low. Taking into account that the ionic radii of chloride is 1.81 and

of bromide 1.96 Å [34], and their molar conductivity values are close the molecular structure of **1** is necessarily very similar to that of **2**. Therefore similar antioxidative capacity was expected for **1** and **2** or somewhat higher efficiency for **1**. The most significant difference between their physicochemical properties is that **1** shows hygroscopicity. Due to the fact that an H-donor group is necessary for DPPH neutralization, might be assumed that this proton originates from the NH_2 substituent of the pyrazole ring. Easy release of H● is important for an efficient radical neutralization [35]. In this regard, the amino substituent of the pyrazole ring has a key role in DPPH radical neutralization and protection from oxidative damage. Considering both of these, similarities and differences between **1** and **2**, the most acceptable explanation of the unexpected low antioxidative capacity of **1** is that the amino H atom is hindered in **1**. Most probably the absorbed water stays bonded to complex **1** even in the methanolic solution that has been used in the protocol of the DPPH assay solution. On the other hand, due to the less ionic radii of chloride compared to bromide, slightly more compact packing of **1** than that of **2** is also possible. In compounds **5** and **2**, the NH_2 group is not hindered, and it may react with the free radical giving to it a H● to neutralize. These compounds do not dissociate in methanolic solution, so their amino H atoms take part in less or weaker intermolecular interactions and those atoms are available for DPPH● neutralization. Dissociation of **3** and **4** in solution change the intramolecular interactions in the complex cations. Therefore, the leaving of the amino H atom is hindered, which leads to the significantly lower antioxidative activity of these compounds. Given that there are no reports on the antioxidant activity of these complexes with zinc as a transition metal, it is very difficult, both from the chemical and biological aspects, to make comparisons with the results of antioxidant activity tested on complexes with some other metal [36]. Generally, it can be concluded that the results of antioxidant activity obtained in this study present a novelty in coordination chemistry and could be of great importance for further studies of biological activity, as well as potential applications of these compounds in foods and pharmaceuticals.
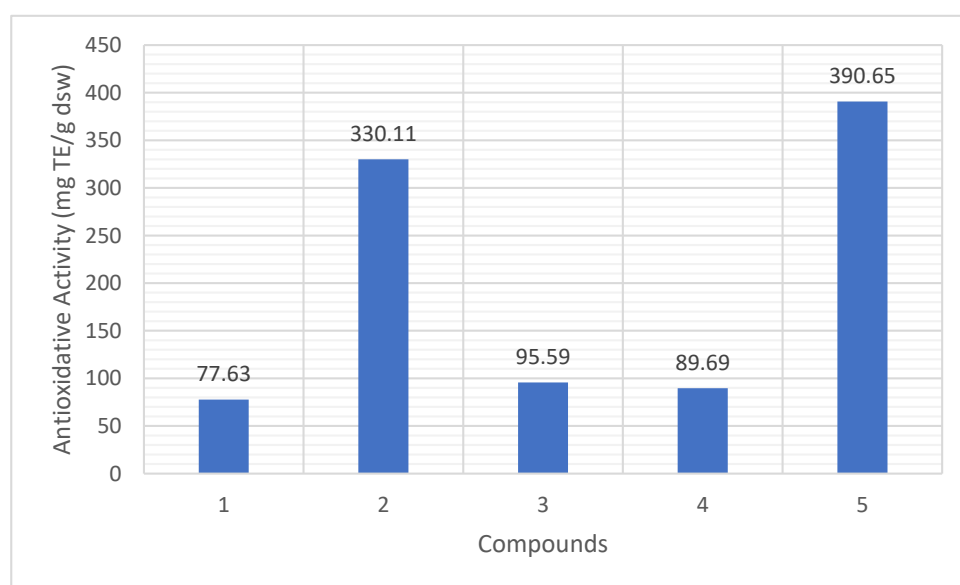

Figure 12. Histogram of complexes' antioxidative activity.

3. Materials and Methods

3.1. Materials and Physical Measurements

All chemicals used were commercial products of analytical reagent grade. Elemental analyses (C, H, N) of air-dried complexes were carried out by standard micromethods in the Center for Instrumental Analyses, ICTM in Belgrade. Molar conductivities of freshly prepared complexes solutions ($c = 1\cdot10^{-3}$ mol dm^{-3}) were measured on a Jenway 4510

conductivity meter (Cole-Parmer, Staffordshire, ST15 OSA, UK). IR spectra were recorded using KBr pellets on a NEXUS 670 FTIR spectrophotometer (Thermo Nicolet, Thermo Fisher Scientific Inc., USA) in the range of 4000–400 cm^{-1}. Thermal data were collected using TA Instruments SDT Q600 thermal analyzer (TA Instrument, New Castle, DE, USA) coupled to Hiden Analytical HPR20/QIC mass spectrometer (Hiden Co., Warrington, UK). The decomposition was followed from room temperature to 500 °C at 10 °C min^{-1} heating rate in argon (flow rate = 50 cm^3 min^{-1}). Sample holder/reference: alumina crucible/empty alumina crucible. Sample mass 2–3 mg. Selected ions between m/z = 1–80 were monitored in multiple ion detection mode (MID).

3.2. Neutralization of DPPH Radical

The synthetic samples were tested for the scavenging effect on the DPPH radical (DPPH●) according to a slightly modified method [37].

DPPH● mimics free radicals species formed in the human body which should be neutralized by the test compounds. DPPH● solution is purple, and the reduction of this free radical leads to the gradual transition of the color to a pale yellow due to the presence of a pycril group [38].

The tested samples dissolved in methanol and a series of concentrations (ranging 0.625–30 mg/mL) have been prepared. The solutions have been tested using 96-well microplates. Ten microliters of the sample's solution were added to the DPPH solution (previously prepared in methanol, 90 µmol/L) and the mixture is diluted with methanol. Blank (the tested sample is substituted with used solvent) and matrix blank (solvent and samples without DPPH solution) probes also have been added. Absorbance at 515 nm is measured after 30 min. The antioxidant activity is expressed as milligrams Trolox equivalents per gram of dry samples weight (mg TE/g dsw).

3.3. Preparation of the Coordination Compounds

3.3.1. Zn(L)$_2$Cl$_2$ (**1**)

The ligand, L (0.169 g; 1 mmol) was dissolved in hot MeOH (10 cm^3) and ZnCl$_2$ (0.068 g; 0.5 mmol) was added. Three days later white microcrystals were filtered and washed with MeOH and Et$_2$O. Yield: 0.123 g (54%). Calcd. (Found) for ZnC$_{14}$H$_{22}$N$_6$O$_4$Cl$_2$ (M = 474.66): C, 35.44; H, 4.67; N, 17.71; (C, 35.12; H, 4.85; N, 17.53). IR bands [$\tilde{v}$/cm^{-1}]: 3484 (sh), 3433 (s), 3337 (s), 3238 (m), 3176 (m), 2981 (m), 2939 (w), 2906 (w), 2874 (w), 1703 (s), 1630 (s), 1557 (s), 1456 (m), 1410 (m), 1383 (m), 1361 (m), 1326 (s), 1306 (m), 1231 (s), 1190 (m), 1172 (m), 1124 (s), 1015 (m), 984 (m), 888 (w), 846 (w), 776 (m), 697 (w), 613 (w), 565 (w). Molar conductivity, Λ (S cm^2 mol^{-1}): 8 (DMF).

3.3.2. [Zn(L)$_2$Br$_2$] (**2**)

The ligand, L (0.169 g; 1 mmol) was dissolved in hot MeOH (10 cm^3) and ZnBr$_2$ (0.113 g; 0.5 mmol) was added. Four days later transparent colorless plate-like single crystals were filtered and washed with MeOH and Et$_2$O. Yield: 0.131 g (47%). Calcd. (Found) for ZnC$_{14}$H$_{22}$N$_6$O$_4$Br$_2$ (M = 563.56): C, 29.82; H, 3.94; N, 14.92. (C, 29.73; H, 3.86; N, 14.77). IR bands [$\tilde{v}$/cm^{-1}]: 3429 (s), 3339 (s), 3234 (m), 3170 (m), 3131 (w), 2982 (m), 2938 (w), 2915 (w), 2874 (w), 1700 (s), 1628 (s), 1557 (s), 1478 (m), 1455 (m), 1444 (m), 1412 (m), 1389 (m), 1360 (w), 1325 (s), 1229 (s), 1188 (m), 1125 (s), 1113 (s), 1017 (m), 983 (s), 885 (w), 846 (m), 779 (s), 703 (w), 689 (w), 611 (w), 565 (m). Molar conductivity, Λ (S cm^2 mol^{-1}): 13 (DMF).

3.3.3. Zn(L)$_2$I$_2$·0.5MeOH (**3**)

The ligand, L (0.169 g; 1 mmol) was dissolved in hot MeOH (10 cm^3) and ZnI$_2$ (0.16 g; 0.5 mmol) was added. Three days later pale-yellow microcrystals were filtered and washed with MeOH and Et$_2$O. Yield: 0.159 g (60%). Calcd. (Found) for ZnC$_{14}$H$_{22}$N$_6$O$_4$I$_2$·0.5CH$_4$O (M = 673.59): C, 25.86; H, 3.59; N, 12.48. (C, 25.60; H, 3.57; N, 12.44). IR bands [$\tilde{v}$/cm^{-1}]: 3440 (s), 3340 (s), 3235 (m), 3172 (w), 3108 (sh), 2981 (m), 2937 (w), 2905 (w), 1697 (s),

1623 (s), 1556 (s), 1455 (m), 1409 (m), 1384 (m), 1361 (w), 1329 (s), 1229 (s), 1190 (m), 1173 (m), 1118 (s), 1013 (m), 982 (m), 888 (w), 846 (w), 782 (m), 694 (w), 614 (w), 563 (w). Molar conductivity, Λ (S cm^2 mol^{-1}): 110 (DMF).

3.3.4. [Zn(L)$_2$(H$_2$O)$_4$](NO$_3$)$_2$ (**4**)

The ligand, L (0.085 g; 0.5 mmol) was dissolved in 5 cm^3 acetone at room temperature and Zn(NO$_3$)$_2$·6H$_2$O (0.074 g; 0.25 mmol) was dissolved in 2 cm^3 acetone upon slight heating. The two solutions were mixed, briefly heated, and diluted with acetone to 10 cm^3. Six days later white platelike single crystals were filtered and washed with acetone. Yield: 0.091 g (30%). Calcd. (Found) for ZnC$_{14}$H$_{22}$N$_8$O$_{10}$·4H$_2$O (M = 599.83): C, 28.03; H, 5.04; N, 18.68; (C, 27.77; H, 5.11; N, 18.50). IR bands [$\tilde{v}$/cm^{-1}]: 3453 (s), 3354 (s), 3243 (sh), 3185 (sh), 2994 (m), 2982 (m), 2940 (w), 2915 (w), 1682 (s), 1657 (s), 1625 (s), 1560 (s), 1479 (w), 1451 (m), 1411 (s), 1384 (vs), 1324 (s), 1228 (s), 1125 (m), 1112 (m), 1043 (w), 1031 (w), 970 (m), 888 (w), 843 (w), 824 (w), 781 (m), 713 (w), 695 (w), 624 (w), 564 (w).

3.3.5. {ZnL(OAc)$_2$}$_2$ (**5**)

The ligand, L (0.169 g; 1 mmol) was dissolved in acetone (4 cm^3) and Zn(OAc)$_2$·2H$_2$O (0.11 g; 0.5 mmol) was added. The mixture was shortly heated and diluted up to 10 cm^3 with acetone. Three days later white microcrystals were filtered and washed with acetone and Et$_2$O.Yield: 0.088 g (34%). Calcd. (Found) for Zn$_2$C$_{22}$H$_{34}$N$_6$O$_{12}$ (M = 705.33): C, 25.86; H, 3.59; N, 12.48. (C, 25.60; H, 3.57; N, 12.44). IR bands [$\tilde{v}$/cm^{-1}]: 3426 (m), 3304 (m), 3240 (m), 3176 (m), 2979 (m), 2936 (w), 1770 (s), 1641 (s), 1603 (s), 1556 (s), 1455 (s), 1401 (s), 1363 (m), 1326 (s), 1189 (m), 1174 (w), 1110 (m), 1058 (w), 1019 (m), 981 (m), 936 (w), 884 (w), 847 (w), 781 (m), 683 (m), 616 (m), 563 (m), and 520 (w). Molar conductivity, Λ (S cm^2 mol^{-1}): 3.5 (DMF).

3.3.6. Crystal Structure Determination

Diffraction experiments were performed at room temperature on a Gemini S diffractometer (Oxford Diffraction) equipped with a Sapphire CCD detector. Data collection control, reflection integration, and data reduction were performed with the CrysAlisPro v. 1.171.39.46 [39]. Crystal structures were solved with the SHELXT [40] and refined with the SHELXL-2018 [41]. The ShelXle was employed as the interface for refinement procedures [42]. Validation of the structural models was performed with the PLATON [43], and Cambridge Structural Database (CSD) by using Mercury CSD [44,45]. Crystallographic data associated with this publication are deposited with the Cambridge Crystallographic Data Centre under the CCDC Numbers 2,141,334–2,141,335 They are available for free at https://www.ccdc.cam.ac.uk/structures, accessed on 11 January 2022. Selected crystallographic and refinement details are presented in Table 4.

Hirshfeld surface analysis was performed with CrystalExplorer21 [46]. For complex **2**, intermolecular interaction energies are calculated for all intermolecular pairs surrounding the Hirshfeld surface of the central molecule using CE-HF model energies [28] and were used for the construction of energy frameworks [47].

Table 4. Selected crystallographic details.

Parameter	[Zn(L)$_2$Br$_2$] (2)	[Zn(L)$_2$(H$_2$O)$_4$](NO$_3$)$_2$ (4)
Crystal data		
Chemical formula	C$_{14}$H$_{22}$Br$_2$N$_6$O$_4$Zn	C$_{14}$H$_{30}$N$_8$O$_{14}$Zn
M_r	563.57	599.83
Crystal system	Monoclinic	Orthorhombic
Space group	$C2/c$	*Ibca*

Table 4. *Cont.*

Parameter	[Zn(L)₂Br₂] (2)	[Zn(L)₂(H₂O)₄](NO₃)₂ (4)
$a/\text{Å}$	14.9764 (6)	7.95140 (10)
$b/\text{Å}$	7.4712 (3)	20.5418 (2)
$c/\text{Å}$	20.3960 (9)	29.7574 (3)
$\beta/°$	91.476 (4)	90
$V/\text{Å}^3$	2281.38 (16)	4860.46 (9)
Z	4	8
Radiation type	Mo $K\alpha$	Cu $K\alpha$
μ/mm^{-1}	4.61	2.17
Crystal size, mm	0.66 × 0.43 × 0.19	0.72 × 0.48 × 0.11
Data collection		
Absorption correction	Multi-scan	Analytical
T_{min}, T_{max}	0.186, 1.000	0.341, 0.797
Measured reflections	9408	11,430
Independent reflections	2646	2317
Observed reflections, $[I > 2\sigma(I)]$	1998	2199
R_{int}	0.029	0.032
$(\sin\theta/\lambda)_{\text{max}}/\text{Å}^{-1}$	0.685	0.609
Refinement		
$R[F^2 > 2\sigma(F^2)]$	0.037	0.028
$wR(F^2)$	0.090	0.080
S	1.02	1.06
No. of reflections	2646	2317
No. of parameters	126	174
$\Delta\rho_{\text{max}}$, $\Delta\rho_{\text{min}}$, e Å^{-3}	0.72, −0.84	0.32, −0.23

4. Conclusions

Five new coordination complexes of ethyl-5-amino-1-methyl-1H-pyrazole-4-carboxylate (**L**) with Zn(II) salts were synthesized. Complexes of the general formula ZnL₂X₂ were obtained in the reaction of methanolic solutions of ZnX₂ (X = Cl, Br, I) and the ligand. ZnL₂I₂ crystallizes with 0.5 MeOH molecule. In the reaction of L with Zn(NO₃)₂·6H₂O in acetone solution, the crystals of [ZnL₂(H₂O)₄](NO₃)₂ were obtained, while the reaction of Zn(OAc)₂·2H₂O and **L** yielded in the formation of a microcrystalline product. Based on the physicochemical characterization of the latter, the formula {ZnL(OAc)₂}₂ is proposed. The compounds obtained from ZnBr₂ and Zn(NO₃)₂·6H₂O crystallized in the form of single crystals and their molecular structure is determined by single crystal XRD. In compound ZnL₂Br₂ (**2**), the tetrahedral environment of the metal center is formed by monodentate coordination of two pyrazole-type ligands via N1, and two bromides. Unlike that, in [ZnL₂(H₂O)₄](NO₃)₂ (**4**), less favorable octahedral surroundings of the Zn(II) center is achieved by monodentate coordination of two pyrazole-type ligands and four water molecules. The complex of the proposed formula {ZnL(OAc)₂}₂ (**5**) is most probably a structural analog of earlier published {CuL(μ-OAc)₂}₂.

The thermal stability of the complexes increases in order **5** < **1** < **2** < **3**< dehydrated **4**. Even though compound [ZnL₂Cl₂] (**1**) does not contain coordinated or lattice water, its thermal stability is lower than that of **2–4** and suggests hygroscopic properties of the complex, which was proved by coupled TG-MS measurements. However, the iodido complex crystallizes with 0.5 molecules of MeOH, which was spontaneously lost during storage. Complex 4 at first lost the coordinated water in two steps, but the dehydrated intermediate follows the trend of thermal and solvolytic stabilities observed in the case of compounds **1–3**. Compound **5** is the thermally less stable complex most probably due to repulsion in its dimeric structure but in DMF it did not dissociate and its lowest molar conductivity value shows that **5** has the highest solvolytic stability.

Considering the physical, chemical, and structural properties of the compounds, most probably the radical-neutralizing group is the amino substituent of the pyrazole ring. Compounds with high solvolytic stability, low molar conductivity (**2** and **5**) show the

highest antioxidative activity. The exception is **1**, with low antioxidative activity. It is most probably caused by more compact packing of **1** in crystal structure and hindered amino substituent of pyrazole-type ligand. Additionally, the other possible reason is H-bond forming between absorbed water molecules and amino substituent. Compounds of low solvolytic stability, ZnL_2I_2 (**3**) and $[ZnL_2(H_2O)_4](NO_3)_2$ (**4**) also show low antioxidative activity. The most probable reason is the change of intermolecular interactions in **3** and **4** by their dissolution. Due to these changes, the amino substituent of the pyrazole-type ligand became hindered for DPPH• radical neutralization.

References

1. Matiadis, D.; Karagiaouri, M.; Mavroidi, B.; Nowak, K.E.; Katsipis, G.; Pelecanou, M.; Pantazaki, A.; Sagnou, M. Synthesis and Antimicrobial Evaluation of a Pyrazoline-Pyridine Silver(I) Complex: DNA-Interaction and Anti-Biofilm Activity. *BioMetals* **2021**, *34*, 67–85. [CrossRef] [PubMed]
2. Allison, D.; Delancey, E.; Ramey, H.; Williams, C.; Alsharif, Z.A.; Al-khattabi, H.; Ontko, A.; Gilmore, D.; Alam, M.A. Synthesis and Antimicrobial Studies of Novel Derivatives of 4-(4-Formyl-3-phenyl-1H-pyrazol-1-yl)Benzoic Acid as Potent Anti-Acinetobacter Baumannii Agents. *Bioorg. Med. Chem. Lett.* **2017**, *27*, 387–392. [CrossRef] [PubMed]
3. Sharshira, E.M.; Hamada, N.M.M. Synthesis and Antimicrobial Evaluation of Some Pyrazole Derivatives. *Molecules* **2012**, *17*, 4962–4971. [CrossRef] [PubMed]
4. Măruțescu, L.; Calu, L.; Chifiriuc, M.C.; Bleotu, C.; Daniliuc, C.G.; Fălcescu, D.; Kamerzan, C.M.; Badea, M.; Olar, R. Synthesis, Physico-Chemical Characterization, Crystal Structure and Influence on Microbial and Tumor Cells of Some Co(II) Complexes with 5,7-Dimethyl-1,2,4-triazolo[1,5-a]pyrimidine. *Molecules* **2017**, *22*, 1233. [CrossRef] [PubMed]
5. Kenchappa, R.; Bodke, Y.D. Synthesis, Analgesic and Anti-Inflammatory Activity of Benzofuran Pyrazole Heterocycles. *Chem. Data Coll.* **2020**, *28*, 100453. [CrossRef]
6. Ragab, F.A.; Abdel Gawad, N.M.; Georgey, H.H.; Said, M.F. Synthesis of Novel 1,3,4-Trisubstituted Pyrazoles as Anti-Inflammatory and Analgesic Agents. *Eur. J. Med. Chem.* **2013**, *63*, 645–654. [CrossRef]
7. Gökhan-Kelekçi, N.; Yabanoğlu, S.; Küpeli, E.; Salgin, U.; Özgen, Ö.; Uçar, G.; Yeşilada, E.; Kendi, E.; Yeşilada, A.; Bilgin, A.A. A New Therapeutic Approach in Alzheimer Disease: Some Novel Pyrazole Derivatives as Dual MAO-B Inhibitors and Antiinflammatory Analgesics. *Bioorg. Med. Chem.* **2007**, *15*, 5775–5786. [CrossRef]
8. Badaweya, E.-S.A.M.; El-Ashmaweyb, I.M. Nonsteroidal Antiinflammatory Agents-Part 1: Antiinflammatory, Analgesic and Antipyretic Activity of Some New 1-(Pyrimidin-2-il)-3-pyrazolin-5-ones and 2-(Pyrimidin-2-yl)-l,2,4,5,6,7-hexahydro-3H-indazol-3-ones. *Eur. J. Med. Chem.* **1998**, *33*, 349–361. [CrossRef]
9. Zhang, D.; Du, P.; Chen, J.; Guo, H.; Lu, X. Pyrazolate-Based Porphyrinic Metal-Organic Frameworks as Catechol Oxidase Mimic Enzyme for Fluorescent and Colorimetric Dual-Mode Detection of Dopamine with High Sensitivity and Specificity. *Sens. Actuators B Chem.* **2021**, *341*, 130000. [CrossRef]
10. Hammouda, M.M.; Metwally, H.M.; Fekri, A.; van der Eycken, J. Synthesis and Molecular Modeling Studies on Novel C2 Alkylated Benzoazonine Scaffold and Corresponding 2-Pyrazoline Derivatives as Acetylcholinestrase Enzyme Inhibitors. *Polycycl. Aromat. Compd.* **2021**, *41*, 1223–1240. [CrossRef]
11. Mede, R.; Gläser, S.; Suchland, B.; Schowtka, B.; Mandel, M.; Görls, H.; Krieck, S.; Schiller, A.; Westerhausen, M. Manganese(I)-Based CORMs with 5-Substituted 3-(2-Pyridyl)pyrazole Ligands. *Inorganics* **2017**, *5*, 8. [CrossRef]

12. Yang, R.; Xu, T.; Fan, J.; Zhang, Q.; Ding, M.; Huang, M.; Deng, L.; Lu, Y.; Guo, Y. Natural Products-Based Pesticides: Design, Synthesis and Pesticidal Activities of Novel Fraxinellone Derivatives Containing N-Phenylpyrazole Moiety. *Ind. Crop. Prod.* **2018**, *117*, 50–57. [CrossRef]

13. Graillot, V.; Tomasetig, F.; Cravedi, J.P.; Audebert, M. Evidence of the in Vitro Genotoxicity of Methyl-pyrazole Pesticides in Human Cells. *Mutat. Res. Genet. Toxicol. Environ. Mutagenes.* **2012**, *748*, 8–16. [CrossRef]

14. da Silva, P.B.; Frem, R.C.G.; Netto, A.V.G.; Mauro, A.E.; Ferreira, J.G.; Santos, R.H.A. Pyrazolyl Coordination Polymers of Cadmium(II). *Inorg. Chem. Commun.* **2006**, *9*, 235–238. [CrossRef]

15. Hosny, N.M. Solvothermal Synthesis, Thermal and Adsorption Properties of Metal-Organic Frameworks Zn and CoZn(DPB). *J. Therm. Anal. Calorim.* **2015**, *122*, 89–95. [CrossRef]

16. Netto, A.V.G.; Frem, R.C.G.; Mauro, A.E.; Crespi, M.S.; Zorel, H.E. Synthesis, Spectral and Thermal Studies on Pyrazolate-bridged Palladium(II) Coordination Polymers. *J. Therm. Anal. Calorim.* **2007**, *87*, 789–792. [CrossRef]

17. Yan, X.Q.; Wang, Z.C.; Qi, P.F.; Li, G.; Zhu, H.L. Design, Synthesis and Biological Evaluation of 2-H-pyrazole Derivatives Containing Morpholine Moieties as Highly Potent Small Molecule Inhibitors of APC–Asef Interaction. *Eur. J. Med. Chem.* **2019**, *177*, 425–447. [CrossRef] [PubMed]

18. Zhao, J.; Jin, B.; Peng, R.; Liu, Q.; Tan, B.; Chu, S. Synthesis and Characterization of a New Energetic Salt 1H-Pyrazole-1-carboxamidine Dinitramide and its Thermal Properties. *J. Therm. Anal. Calorim.* **2016**, *124*, 1431–1439. [CrossRef]

19. Serushkin, V.; Sinditskii, V.P.; Hoang, T.H.; Filatov, S.A.; Shipulina, A.S.; Dalinger, I.L.; Shakhnes, A.K.; Sheremetev, A.B. Thermal and Combustion Behavior of Novel Oxygen-Rich Energetic Pyrazoles. *J. Therm. Anal. Calorim.* **2018**, *132*, 127–142. [CrossRef]

20. Barta Holló, B.; Vojinović Ješić, L.S.; Radanović, M.M.; Rodić, M.; Jaćimović, Ž.K.; Mészáros Szécsényi, K. Synthesis, Physicochemical, and Thermal Characterization of Coordination Compounds of Cu(II) with a Pyrazole-Type Ligand. *J. Therm. Anal. Calorim.* **2020**, *142*, 451–460. [CrossRef]

21. Jaćimović, Ž.K.; Giester, G.; Kosović, M.; Bogdanović, G.A.; Novaković, S.B.; Leovac, V.M.; Latinović, N.; Barta Holló, B.; Mészáros Szécsényi, K. Pyrazole-Type Complexes with Ni(II) and Cu(II): Solvent Exchange Reactions in Coordination Compounds. *J. Therm. Anal. Calorim.* **2017**, *127*, 1501–1509. [CrossRef]

22. Jaćimović, Ž.; Kosović, M.; Kastratović, V.; Barta Holló, B.; Mészáros Szécsényi, K.; Szilágyi, I.M.; Latinović, N.; Vojinović-Ješić, L.; Rodić, M. Synthesis and Characterization of Copper, Nickel, Cobalt, Zinc Complexes with 4-Nitro-3-Pyrazolecarboxylic Acid Ligand. *J. Therm. Anal. Calorim.* **2018**, *133*, 813–821. [CrossRef]

23. Mészáros Szécsényi, K.; Leovac, V.M.; Jaćimović, K.; Češljević, V.I.; Kovács, A.; Pokol, G. Transition Metal Complexes with Pyrazole-Based Ligands Part 12. Characterisation and Thermal Decomposition of $CuCl_2$ Complexes with Di- and Trisubstituted Pyrazoles. *J. Therm. Anal. Calorim.* **2001**, *66*, 573–581. [CrossRef]

24. Geary, W.J. The Use of Conductivity Measurements in Organic Solvents for the Characterisation of Coordination Compounds. *Coord. Chem. Rev.* **1971**, *7*, 81–122. [CrossRef]

25. Yang, L.; Powell, D.R.; Houser, R.P. Structural Variation in Copper(I) Complexes with Pyridylmethylamide Ligands: Structural Analysis with a New Four-Coordinate Geometry Index, T4. *Dalton Trans.* **2007**, 955–964. [CrossRef] [PubMed]

26. Gavezzotti, A. The "Sceptical Chymist": Intermolecular Doubts and Paradoxes. *CrystEngComm* **2013**, *15*, 4027–4035. [CrossRef]

27. Edwards, A.J.; Mackenzie, C.F.; Spackman, P.R.; Jayatilaka, D.; Spackman, M.A. Intermolecular Interactions in Molecular Crystals: What's in a Name? *Faraday Discuss.* **2017**, *203*, 93–112. [CrossRef]

28. Mackenzie, C.F.; Spackman, P.R.; Jayatilaka, D.; Spackman, M.A. *CrystalExplorer* Model Energies and Energy Frameworks: Extension to Metal Coordination Compounds, Organic Salts, Solvates and Open-Shell Systems. *IUCrJ* **2017**, *4*, 575–587. [CrossRef]

29. Nakamoto, K. *Infrared and Raman Spectra of Inorganic and Coordination Compounds Part B*; John Wiley & Sons: Hoboken, NJ, USA, 2008; pp. 64–79.

30. Günzler, H.; Gremlich, H.U. *IR-Spektroskopie: Eine Einführung*, 4th Croatian ed.; Školska Knjiga: Zagreb, Croatia, 2006; pp. 166–194.

31. Győryová, K.; Balek, V. Thermal Stability of New Zinc Acetate-Based Complex Compounds. *J. Therm. Anal. Calorim.* **1993**, *40*, 519–532. [CrossRef]

32. NIST WebBook. Available online: https://webbook.nist.gov/ (accessed on 1 October 2021).

33. Keter, F.K.; Darkwa, J. Perspective: The Potential of Pyrazole-Based Compounds in Medicine. *BioMetals* **2012**, *25*, 9–21. [CrossRef]

34. Shannon, R.D. Revised Effective Ionic Radii and Systematic Studies of Interatomie Distances in Halides and Chaleogenides. *Acta Crystallogr. Sect. A Cryst. Phys. Diffr. Theor. Gen. Crystallogr.* **1976**, *32*, 751–767. [CrossRef]

35. Mollanejad, K.; Asghari, S.; Jadidi, K. Diastereoselective Synthesis of Pyrrolo[1, 2-c]Imidazoles Using Chiral Thiohydantoins, Malononitrile, and Aldehydes and Evaluation of Their Antioxidant and Antibacterial Activities. *J. Heterocycl. Chem.* **2020**, *57*, 556–564. [CrossRef]

36. Amir, A.; Kadhum, H.; Mohamad, A.B.; Al-Amiery, A.A.; Takriff, M.S. Molecules Antimicrobial and Antioxidant Activities of New Metal Complexes Derived from 3-Aminocoumarin. *Molecules* **2011**, *16*, 6969–6984. [CrossRef]

37. Vlaisavljević, S.; Jelača, S.; Zengin, G.; Mimica-Dukić, N.; Berežni, S.; Miljić, M.; Dajić Stevanović, Z. Alchemilla Vulgaris Agg. (Lady's Mantle) from Central Balkan: Antioxidant, Anticancer and Enzyme Inhibition Properties. *RSC Adv.* **2019**, *9*, 37474–37483. [CrossRef]

38. Munteanu, I.G.; Apetrei, C.; Hadjipavlou-Litina, D. Analytical Methods Used in Determining Antioxidant Activity: A Review. *Int. J. Mol. Sci.* **2021**, *22*, 3380. [CrossRef]

39. Rigaku Oxford Diffraction. *CrysAlisPro Software System*; Rigaku Corporation: Wroclaw, Poland, 2019.

40. Sheldrick, G.M. SHELXT-Integrated Space-Group and Crystal-Structure Determination. *Acta Crystallogr. Sect. A Found. Adv.* **2015**, *71*, 3–8. [CrossRef]

41. Sheldrick, G.M. Crystal Structure Refinement with *SHELXL. Acta Crystallogr. Sect. C Struct. Chem.* **2015**, *71*, 3–8. [CrossRef]

42. Hübschle, C.B.; Sheldrick, G.M.; Dittrich, B. ShelXle: A Qt Graphical User Interface for SHELXL. *J. Appl. Cryst.* **2011**, *44*, 1281–1284. [CrossRef]

43. Spek, A.L. Structure Validation in Chemical Crystallography. *Acta Crystallogr. Sect. D Biol. Crystallogr.* **2009**, *65*, 148–155. [CrossRef]

44. Groom, C.R.; Bruno, I.J.; Lightfoot, M.P.; Ward, S.C. The Cambridge Structural Database. *Acta Crystallogr. Sect. B Struct. Sci. Cryst. Eng. Mater.* **2016**, *72*, 171–179. [CrossRef]

45. Macrae, C.F.; Sovago, I.; Cottrell, S.J.; Galek, P.T.A.; McCabe, P.; Pidcock, E.; Platings, M.; Shields, G.P.; Stevens, J.S.; Towler, M.; et al. Mercury 4.0: From Visualization to Analysis, Design and Prediction. *J. Appl. Cryst.* **2020**, *53*, 226–235. [CrossRef] [PubMed]

46. Spackman, P.R.; Turner, M.J.; McKinnon, J.J.; Wolff, S.K.; Grimwood, D.J.; Jayatilaka, D.; Spackman, M.A. CrystalExplorer: A Program for Hirshfeld Surface Analysis, Visualization and Quantitative Analysis of Molecular Crystals. *J. Appl. Cryst.* **2021**, *54*, 1006–1011. [CrossRef] [PubMed]

47. Turner, M.J.; Thomas, S.P.; Shi, M.W.; Jayatilaka, D.; Spackman, M.A. Energy Frameworks: Insights into Interaction Anisotropy and the Mechanical Properties of Molecular Crystals. *Chem. Commun.* **2015**, *51*, 3735–3738. [CrossRef] [PubMed]